Available online at www.sciencedirect.com
ScienceDirect
International Journal of Multiphase Flow 34 (2008) 363–374
International Journal of Multiphase Flow
www.elsevier.com/locate/ijmulflow

Phase and velocity distributions in vertically upward high-viscosity two-phase flow

J. Schmidt [a,*], H. Giesbrecht [a], C.W.M. van der Geld [b]

[a] BASF AG, GCT/S-L511, D-67056 Ludwigshafen, Germany
[b] Technische Universiteit Eindhoven, P.O. Box 513, 5600 MB, Eindhoven, The Netherlands

Received 17 November 2006; received in revised form 30 August 2007

Dedicated to the 65th birthday of Prof. Lutz Friedel, TU Hamburg-Harburg, Germany.

Abstract

The two-phase pressure drop in vertical industrial pipes is mainly determined by gravitation and acceleration of the fluid, which means that the void fraction is key an important parameter in any model to predict pressure drops. Typically, these models are applied in industry to size pumps and, e.g., emergency relief systems. There is a shortage of void fraction data in the literature for liquids with a dynamic viscosity above 1000 mPa s. Adiabatic experiments have been performed of mixtures of nitrogen and solutions of polyvinylpyrrolidone (Luviskol®) in water with dynamic viscosities in the range 900–7000 mPa s. Inner tube diameter was 54.5 mm. Mass flux and quality were varied in a wide range: 8–3500 kg/m^2/s and 0–82%, respectively. The corresponding superficial velocities were 0.005–3.4 m/s for the liquid and 0–30 m/s for the nitrogen. For comparison, reference measurements were taken of mixtures of nitrogen with water (1 mPa s). Care has been taken to measure only well-developed flows.

Time-averaged local void fraction profiles have been determined with a linearly traversed γ-ray densitometer. Analysis shows that at high superficial gas velocity (gas Reynolds numbers in the range 0–1.2 $\times$ 10^5 have been studied, liquid Reynolds numbers in the range 0.2–1.7 $\times$ 10^5) the total superficial velocity profile is peaking in the centre of the tube. With increasing superficial gas velocity the peaking gets stronger.

It is shown that time- and space-averaged void fractions are not well predicted with existing correlations. Two new correlations are presented, one of them in terms of the distribution parameter. The other, in terms of the velocity slip, unifies the results of low- and high-viscosity mixtures.

Keywords: Void fraction measurements; Flow pattern; Two-phase; Viscous liquid; Distribution phenomena; Void fraction correlations

1. Introduction

The emergency relief of chemical reactors often leads to a discharge of gas and liquid with a high viscosity. In polymer processing plants viscosities up to 100 Pa s have to be handled. For the sizing of safety devices and outlet pipe systems, a model to predict the void fraction is of prime importance. Another application area of the present work is the prediction of static head in industrial pipe systems. The two-phase density and pressure drop depend largely on the void fraction. However, current models for flow pattern and void fraction were merely experimentally validated for oil-like fluids and water with glycerine, i.e. for viscosities of up to 0.055 Pa s (Chisholm, 1983; Diener and Friedel, 1998; Mayinger, 1982; Spedding et al., 1998; McNeil and Stuart, 2003). These experiments are discussed below.

In the literature, only few void fraction measurements are reported of liquids with a high viscosity. Spisak and Idzik (1994) measured the void fraction for slug flow in vertical glass tubes of 25 mm diameter with a mixture of air

* Corresponding author. Tel.: + 49 1728763561; fax: +49 6321489816.
E-mail addresses: juergen.schmidt@onlinehome.de (J. Schmidt), c.w.m.v.d.geld@tue.nl (C.W.M. van der Geld).

0301-9322/$ - see front matter © 2007 Elsevier Ltd. All rights reserved.
doi:10.1016/j.ijmultiphaseflow.2007.10.013

and lubricating oils with a dynamic viscosity, μ_L, up to 4.8 Pa s. They compared their data with models of Lockhart and Martinelli (1949) and of other people, but the agreement found is poor. Kabir and Hasan (1990) investigated flow patterns and pressure drop in gas/oil wells for some commercially available oil. No comparison between measured void fractions and fractions predicted with existing correlations or their new empirical equation was given. Measurements of the film thickness of annular flow in a vertical tube of 26 mm diameter with air and a glycerol/water solution with $\mu_L = 0.007$ Pa s were made by Fukano and Furukawa (1998). No attempt was made to extract the void fraction and correlate with a model. McNeil and Stuart (2003) measured water and glycerine solutions with nominal liquid viscosities up to 0.055 Pa s. Only annular flow was found, and a prediction method developed that only applies to this flow regime.

Existing empirical correlations are often in terms of the velocity slip and use the liquid dynamic viscosity as an input parameter, viz. Lockhart and Martinelli (1949), Premoli et al. (1971), Chisholm (1962, 1983), Claxton et al. (1972). These models were generally fitted to a limited set of data of two-phase flow with a liquid viscosity below 0.03 Pa s. Despite that a comparison of these models with new high viscosity data will be made in this report. No further experimental data have been found outside this range.

The present paper presents void fraction distributions and flow-patterns measured in cocurrent upflow in a vertical pipe of mixtures of gas and fluid with viscosities up to 7 Pa s. Mass qualities up to 82% and mass fluxes up to 3500 kg/m^2 s^{-1} could be realized in a special test rig at BASF, Ludwigshafen, Germany. Void fraction profiles are measured with γ-ray densitometry. Measured distribution coefficients are analyzed with the aid of the void fraction profiles. The applicability of existing correlations from the literature for the mean void fraction is investigated. New correlations for the average void fraction are presented. The consequences for the profile of the total superficial velocity in the pipe are discussed.

2. Experimental set-up

The investigations were performed in the test rig depicted in Fig. 1. The liquid phase was pumped by a gear wheel pump to the mixer where it was brought into contact with the gas phase in the form of a film close to the wall. Downstream of the mixer a grid was installed providing for intense mixing of the two phases. The actual test section consisted of a vertical pipe of $D = 54.5$ mm inner diameter with seven pressure taps beginning 2.2 m downstream of the mixer and ending an additional 3.1 m further downstream. A glass pipe downstream of the test section enabled visual observation of the flow pattern. All but the valve V2 are ball valves with a smooth throughput. It was verified whether the flow was fully developed at the measuring location by measuring void fraction profiles at two axial positions. The axial position of the densitometer was changed from 2.9 m downstream of the mixer outlet (see Fig. 1) to 3.5 m; differences found turned out to be less than the measurement error. The pressure in the test section could be adjusted by the throttling valve V2 (Fig. 1) at the end of the pipe system. After expansion to ambient pressure with escape of most of the gas phase the liquid could be directed

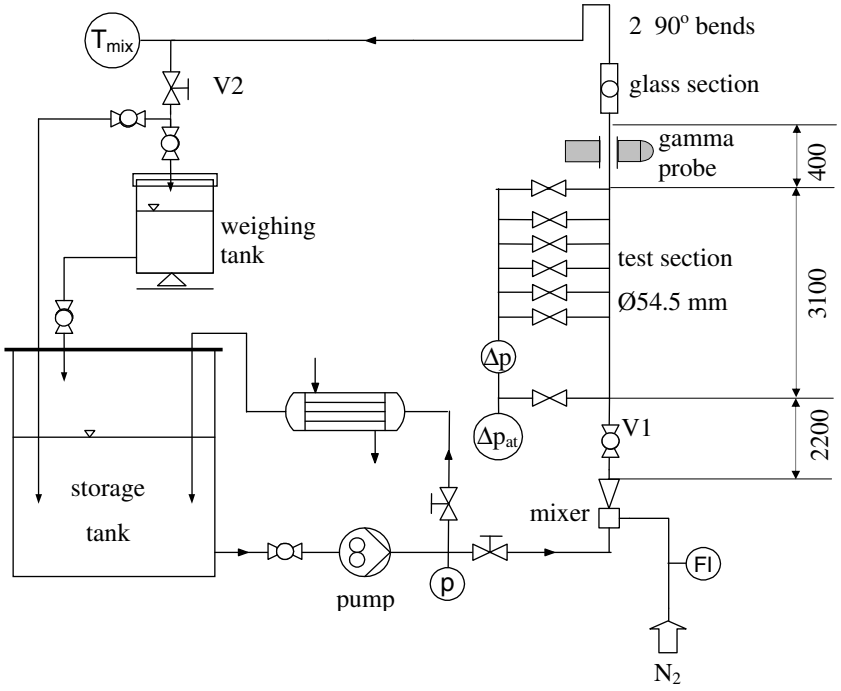

Fig. 1. Schematic of the test rig.

either into a weighing tank or directly into the storage tank. The liquid mass flow rate measurement was calibrated by weighing the spill of single phase liquid during 10 s, leading to an error of less than 2%. However, during two-phase operation fluctuations in the feed of liquid occurred, causing the net error in the liquid mass flow rate to be about 4%.

Nitrogen from the central supply network was taken as the gas phase. Its flow rate was measured with two Rotameters with an accuracy of 2% each. The mass density of the gas is of course calculated at the appropriate pressure and temperature. The liquid phase consisted of solutions of PVP (polyvinylpyrrolidone, BASF product name Luviskol®) and water with viscosities in the range of $\mu_L = 0.001$–7 Pa s. The liquid viscosities have been measured with a rotating cup viscosimeter as a function of temperature and shear rate. Mass densities were measured by weighing calibrated cylinders, surface tension with a so-called G10 measuring system (drop shape analysis). Samples were taken both at the beginning and at the end of a measurement run; variation during a test series is typically less than 5% for the liquid viscosity. Only average values are used to indicate a measuring condition, and it was made sure that no micro-bubbles occurred in the samples. The micro-bubbles result from the mixing of two phases, liquid and nitrogen. It took quite a while to obtain steady state conditions in the test section and storage vessel, but as a result the content of micro-bubbles in the feed of the test section was constant. In order to avoid excessive foaming in the storage tank less than 0.1 wt.% of an anti-foaming agent was added (Afranil T), which reduced the surface tension considerably (for example from 66 to 36 mN/m). Within the range of measurements except for the highest gas flow rates the solutions behaved like Newtonian fluids.

The void fraction was determined from the signal of a γ-ray densitometer consisting of a Cs^{137} radiation source with strength of 10 GBq on one side of the pipe and a detection unit on the opposite side. Both devices were mounted upon a common support which could be shifted with high precision (0.05 mm) orthogonal to the axis of the test pipe. The γ-beam was restricted by a rectangular orifice of 2 mm width and 20 mm height. The frequency signal from the counter of the γ-densitometer – being a measure for the radiation intensity I – was stored in the data acquisition system with a sampling rate of 100–500 Hz. The radiation intensity I of γ-rays passing through absorbing material is attenuated according to the Lambert–Beer-law $\mathrm{d}I/I = -\tilde{\mu} \cdot \rho \cdot \mathrm{d}y$, where ρ denotes the fluid mass density, $\mathrm{d}y$ the differential path length and $\tilde{\mu}$ the attenuation coefficient. Let x denote the transverse coordinate in a Cartesian coordinate system in a cross-sectional plane normal to the tube axis; x is taken to be zero in the centre of the tube, see Fig. 2. Measured radiation intensities yield the time and line averaged void fraction $\varepsilon_y(x)$

$$\varepsilon_y(x) = \ln\frac{I/I_0}{I_L/I_0} \Big/ \ln\frac{I_G/I_0}{I_L/I_0} \tag{1}$$

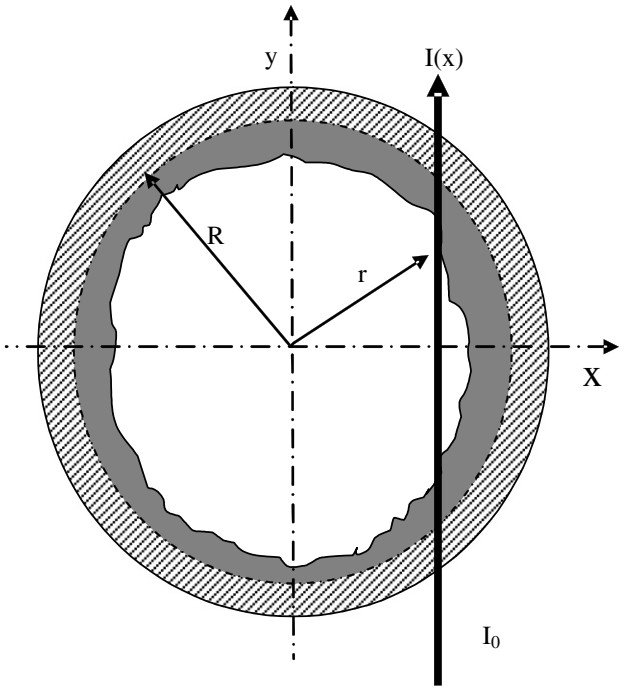

Fig. 2. Schematic of coordinate system and a chordal beam of the gamma densitometer.

Herein I_G and I_L are the radiation intensities from experiments when the pipe is filled with gas or liquid only, and I_0 is the incident radiation intensity. At each position an average of the I/I_0-signal over about 8200 samples was taken, whereas values of I_G/I_0 and I_L/I_0 were determined from calibration measurements with even higher accuracy. The accuracy of the densitometer measurements is mainly determined by the number of samples taken and the thickness of the pipe wall encountered by the beam. The absolute error in the void fraction depends mainly on radiation fluctuations and Poisson statistics and is estimated in a way described by Shollenberger et al. (1997) to be 5% near the wall and 3% in the centre.

Integration of the transverse profile $\varepsilon_y(x)$ across the whole diameter D, from radial position $-R$ to R, where R is the tube radius, yields the cross-sectional average of the time-averaged void fraction, ε (Fig. 2)

$$\begin{aligned}\varepsilon &= \frac{2}{\pi \cdot R^2} \cdot \int_{-R}^{+R} \varepsilon_y(x) \cdot y(x) \cdot \mathrm{d}x \\ &= \frac{2}{\pi \cdot R^2} \cdot \int_{-R}^{+R} \varepsilon_y(x) \cdot \sqrt{R^2 - x^2} \cdot \mathrm{d}x \end{aligned} \tag{2}$$

The last term in Eq. (2) defines the length y; y is half the ray length within the pipe (see Fig. 2). In this paper only time-averaged quantities are considered. In the following, local time-averaged quantities will be marked with an asterisk. Cross-sectional averaged quantities are calculated in the usual way

$$\Omega = \langle \Omega^* \rangle = \frac{1}{A} \int \int_A \Omega^*(x,y) \cdot \mathrm{d}x\,\mathrm{d}y; \quad \Omega = \varepsilon; j, j_G, j_L \tag{3}$$

Table 1
Parameter ranges for the new measurements of gas–liquid upward two-phase flow

$\dot{m}_L$ [kg/h]	$\dot{m}_G$ [kg/h]	ρ_L [kg/m^3]	ρ_G [kg/m^3]	μ_L [Pa s]	$\dot{x}$ [–]	j_L [m/s]	j_G [m/s]
40–29026	0–329	982–1094	0.91–2.29	0.001–6.88	0–0.82	0.005–3.4	0–30

The accuracy of the mean void measurements with the γ-densitometer is checked by comparison with the following variant of the quick-closing valves method. Valve V1 at the entrance to the test section (see Fig. 1) is suddenly closed, while the 90° bend at the exit, downstream of the glass section, closes the test section in a natural way. Backflow from the *U*-bend is taken into account. These "mouse trap" measurements are in agreement with the mean void fractions determined with the γ-densitometer within a relative uncertainty of about 10%.

Table 1 shows the range of the test parameters; here $\dot{x}$ denotes the mass flow quality, $\dot{m}_G/(\dot{m}_G + \dot{m}_L)$. The measurements performed in the experimental set-up provide both local void and flow distribution profiles (Section 3) and averaged void fraction data (Sections 4 and 5).

3. Void fraction distributions: results and deductions regarding the velocity profile

In total, 87 data points have been collected, each one yielding both a void fraction profile and an averaged void fraction of the two-phase flow, see Table 2. In this section distribution results are presented and analyzed. In Sections 4 and 5, mean void fractions will be presented, as well as two new correlations to predict them.

3.1. Axial/radial void distributions: flow patterns

From visual observation of the flow in the glass section of the test pipe the flow patterns have been identified for certain flow conditions. Judgement of the variations in time of the signal of the γ-densitometer provided further evidence of the flow pattern present. Fig. 3 shows the flow pattern map for $\mu_L \approx 1.6$ Pa s. In comparison to flow charts for air/water flow of the well known map of Taitel et al. (1980), the transition to annular flow is generally shifted towards lower superficial gas velocities. A similar behaviour has been found by Taitel et al. for experiments with natural gas and crude oil. Typically, micro-bubbles occur in the liquid of the storage tank, which are difficult to be removed from the liquid without heating or evacuation. It is therefore likely that micro-bubbles also occur in the liquid layer at the wall of annular flows.

3.2. Radial void fraction distributions

The measured chordal beam averages depend on radial (transversal) distance, x, see Figs. 2 and 4. As stated in Section 2, only time-averaged quantities in a vertical pipe are considered in this paper. It is reasonable to assume that the well-developed time-averaged two-phase flows measured are axisymmetric. Direct measurements of local void fraction and velocity distributions are generally rather difficult and/or expensive. They can alternatively be deduced from the measured line averaged values of $\varepsilon_y(x)$ if symmetry around the axis of the vertical tube may be assumed. As an introduction to a new approximate method, an exact way to transform the line averages into radial void fraction distributions is revisited below. The easy and convenient approximate way to perform this transformation is subsequently discussed. This section concludes with some typical profiles obtained for high-viscosity two-phase mixtures.

Fig. 4 shows the dependency of the measured line-averaged void fraction profiles on superficial gas velocity, for a liquid viscosity of $\mu_L = 1.6$ Pa s. The line-averaged void fraction is related to the radial profile $\varepsilon^*(r)$ by, see also Fig. 2,

$$\varepsilon_y(x) = \frac{1}{\sqrt{R^2 - x^2}} \int_x^R \varepsilon^*(r) \cdot \frac{r}{\sqrt{r^2 - x^2}} \cdot \mathrm{d}r = \frac{h(x)}{\sqrt{R^2 - x^2}} \tag{4}$$

The last equality defines the function $h(x)$; note that this h directly follows from $\varepsilon_y(x)$. Direct, exact evaluation of the profile $\varepsilon^*(r)$ is possible with this h using the following expression, which was derived with the Weyl transformation (van der Geld, 1987; Shollenberger et al., 1997):

$$\varepsilon^*(r) = -\frac{1}{\pi} \int_r^R \left.\frac{\partial h}{\partial x}\right|_t \cdot \frac{1}{\sqrt{t^2 - r^2}} \cdot \mathrm{d}t \tag{5}$$

Eq. (5) gives the profile $\varepsilon^*(r)$ upon substitution of the measured $h(x)$-values. Actual assessment can be done with the aid of a cubic spline fit through the measured values of $\varepsilon_y(x)$. Other ways to extract the local void fraction profile are offered by tomographic imaging, see for example Farrell (1981) and Cormack (1983). Tomographic imaging has found commercial application to the measurement of concentrations in two-phase flows of various kinds.

There is a simple and straightforward alternative reduction method possible if the experimental data of $\varepsilon_y(x)$ can be fitted by a power law function of the following form:

$$\varepsilon_y(x) = \varepsilon_{y,\max}\left(1 - \left(\frac{x}{x_{\max}}\right)^2\right)^m \tag{6}$$

Herein $x_{\max}$ is the distance from the centre axis to the surface of the liquid film at the wall. The value of $x_{\max}$ is of course directly observable from the measurements, see Fig. 4. Within the liquid film, when x exceeds $x_{\max}$, $\varepsilon_y(x)$ is zero by definition. In Eq. (6), $\varepsilon_{y,\max}$ is the measured line averaged void fraction through the centre axis, whereas m is a constant that is typically in the range 0.7–1. The profiles of Fig. 4 are all fairly well described by a relation of the form (6). The better the fit, the higher the accuracy of this reduction method is. It is noted that George et al. (2001) used a fourth order

Table 2
Survey of test conditions and results

No.	Mass flux [kg/m^2 s^{-1}]	Quality [–]	μ_L [Pa s]	ρ_L [kg/m^3]	ρ_G [kg/m^3]	j_L [kg/m^3]	j_G [kg/m^3]	ε [–]	Mixture
1	95.1	0.00128	0.001	996.6	1.22	0.10	0.10	0.23	N_2/water
2	96.3	0.01339	0.001	996.7	0.91	0.10	1.42	0.67	N_2/water
3	100.0	0.05054	0.001	996.7	1.27	0.10	3.99	0.81	N_2/water
4	113.9	0.16593	0.001	996.6	1.34	0.10	14.11	0.92	N_2/water
5	132.2	0.28167	0.001	997.4	1.50	0.10	24.81	0.96	N_2/water
6	1084.5	0.00011	0.001	997.0	1.15	1.09	0.11	0.09	N_2/water
7	1072.7	0.00113	0.001	997.1	1.25	1.07	0.96	0.42	N_2/water
8	1138.2	0.00581	0.001	997.4	1.25	1.13	5.27	0.72	N_2/water
9	1073.6	0.01794	0.001	997.5	1.28	1.06	15.02	0.84	N_2/water
10	1011.1	0.03770	0.001	997.9	1.36	0.98	28.12	0.89	N_2/water
11	3163.4	0.00004	0.001	997.5	1.35	3.17	0.09	0.03	N_2/water
12	3104.5	0.00039	0.001	997.3	1.18	3.11	1.02	0.27	N_2/water
13	3059.4	0.00247	0.001	996.9	1.38	3.06	5.46	0.59	N_2/water
14	3025.5	0.00654	0.001	996.9	1.54	3.02	12.86	0.75	N_2/water
15	2871.2	0.01322	0.001	997.2	1.74	2.84	21.76	0.82	N_2/water
16	1017.5	0.00012	0.001	997.4	1.31	1.02	0.09	0.06	N_2/water
17	1021.2	0.00117	0.001	997.2	1.24	1.02	0.96	0.39	N_2/water
18	1049.3	0.00604	0.001	997.0	1.21	1.05	5.24	0.70	N_2/water
19	1040.9	0.01804	0.001	997.3	1.23	1.02	15.27	0.84	N_2/water
20	1062.7	0.03640	0.001	997.4	1.31	1.03	29.58	0.90	N_2/water
21	99.1	0.00123	1.15	1054.3	1.34	0.09	0.09	0.18	N_2/Luviskol
22	99.0	0.00505	1.13	1053.8	1.23	0.09	0.41	0.36	N_2/Luviskol
23	110.8	0.01163	1.16	1054.4	1.27	0.10	1.02	0.41	N_2/Luviskol
24	125.0	0.04000	1.09	1053.5	1.24	0.11	4.02	0.51	N_2/Luviskol
25	1081.3	0.00013	1.10	1053.8	1.47	1.03	0.09	0.05	N_2/Luviskol
26	1083.4	0.00031	1.08	1053.4	1.52	1.03	0.22	0.11	N_2/Luviskol
27	967.7	0.00140	1.08	1053.6	1.66	0.92	0.82	0.17	N_2/Luviskol
28	1148.3	0.00265	1.09	1053.5	1.55	1.09	1.96	0.35	N_2/Luviskol
29	1067.4	0.01715	1.09	1053.7	1.90	1.00	9.65	0.50	N_2/Luviskol
30	982.2	0.03994	1.13	1054.0	2.26	0.89	17.36	0.56	N_2/Luviskol
31	3130.1	0.00008	1.09	1053.9	1.82	2.97	0.14	0.03	N_2/Luviskol
32	3202.7	0.00045	1.04	1053.5	1.97	3.04	0.73	0.10	N_2/Luviskol
33	3240.4	0.00555	1.09	1053.9	1.64	3.06	11.00	0.38	N_2/Luviskol
34	3246.2	0.01193	1.05	1053.6	1.40	3.04	27.66	0.45	N_2/Luviskol
35	1994.0	0.00060	1.17	1052.7	1.76	1.89	0.68	0.14	N_2/Luviskol
36	2005.6	0.00327	1.16	1052.6	2.05	1.90	3.21	0.33	N_2/Luviskol
37	433.1	0.03788	0.98	1016.0	1.43	0.41	11.45	0.57	N_2/Luviskol
38	2171.7	0.00322	1.15	1052.6	1.92	2.06	3.64	0.35	N_2/Luviskol
39	3456.1	0.00004	1.13	1052.4	1.97	3.28	0.07	0.02	N_2/Luviskol
40	3408.1	0.00035	0.97	1013.4	2.03	3.36	0.59	0.09	N_2/Luviskol
41	3363.6	0.00088	0.87	982.0	2.12	3.42	1.40	0.17	N_2/Luviskol
42	109.4	0.16768	1.21	1054.7	1.41	0.09	13.01	0.65	N_2/Luviskol
43	149.4	0.24888	1.25	1055.1	1.54	0.11	24.08	0.73	N_2/Luviskol
44	11.3	0.01053	1.21	1053.0	1.46	0.01	0.08	0.27	N_2/Luviskol
45	12.6	0.09434	1.32	1053.6	1.59	0.01	0.75	0.44	N_2/Luviskol
46	462.5	0.00026	1.22	1053.0	1.40	0.44	0.09	0.08	N_2/Luviskol
47	82.6	0.01441	1.24	1053.1	1.51	0.08	0.79	0.40	N_2/Luviskol
48	131.8	0.00452	1.30	1053.5	1.50	0.12	0.40	0.33	N_2/Luviskol
49	595.2	0.00200	1.24	1053.1	1.36	0.56	0.88	0.30	N_2/Luviskol
50	487.0	0.01332	1.19	1052.8	1.37	0.46	4.73	0.47	N_2/Luviskol
51	2065.7	0.00006	1.23	1053.1	1.58	1.96	0.08	0.02	N_2/Luviskol
52	2201.7	0.00007	1.24	1053.1	1.86	2.09	0.08	0.02	N_2/Luviskol
53	2225.9	0.00053	1.20	1052.9	1.60	2.11	0.74	0.14	N_2/Luviskol
54	2106.0	0.00837	1.24	1053.1	2.29	1.98	7.69	0.44	N_2/Luviskol
55	15.2	0.41360	1.42	1054.1	1.64	0.01	3.83	0.57	N_2/Luviskol
56	18.7	0.74555	1.90	1056.0	1.67	0.00	8.36	0.69	N_2/Luviskol
57	44.1	0.75728	2.08	1056.5	1.52	0.01	21.95	0.77	N_2/Luviskol
58	108.6	0.00066	1.34	1053.7	1.36	0.10	0.05	0.11	N_2/Luviskol
59	113.1	0.00105	1.33	1053.6	1.37	0.11	0.09	0.17	N_2/Luviskol
60	91.5	0.00130	1.42	1054.1	1.31	0.09	0.09	0.17	N_2/Luviskol
61	97.2	0.01224	1.36	1053.8	1.22	0.09	0.98	0.41	N_2/Luviskol
62	106.1	0.06481	1.42	1054.1	1.26	0.09	5.47	0.54	N_2/Luviskol
63	136.1	0.13884	1.42	1054.1	1.53	0.11	12.36	0.64	N_2/Luviskol

(*continued on next page*)

Table 2 (*continued*)

No.	Mass flux [kg/m^2 s^{-1}]	Quality [–]	μ_L [Pa s]	ρ_L [kg/m^3]	ρ_G [kg/m^3]	j_L [kg/m^3]	j_G [kg/m^3]	ε [–]	Mixture
64	549.4	0.06501	1.37	1053.9	1.91	0.49	18.73	0.63	N_2/Luviskol
65	441.3	0.00027	1.33	1052.8	1.30	0.42	0.09	0.08	N_2/Luviskol
66	390.2	0.00305	1.37	1053.2	1.23	0.37	0.96	0.34	N_2/Luviskol
67	533.2	0.01493	1.34	1053.0	1.35	0.50	5.91	0.48	N_2/Luviskol
68	393.7	0.04617	1.35	1053.1	1.43	0.36	12.70	0.57	N_2/Luviskol
69	453.5	0.07931	1.45	1054.0	1.63	0.40	22.10	0.65	N_2/Luviskol
70	17.6	0.00676	3.81	1090.4	1.21	0.02	0.10	0.28	N_2/Luviskol
71	8.3	0.14286	3.52	1089.9	1.54	0.01	0.77	0.43	N_2/Luviskol
72	16.9	0.36664	4.37	1091.4	1.53	0.01	4.05	0.53	N_2/Luviskol
73	31.2	0.61187	5.29	1092.8	1.50	0.01	12.79	0.65	N_2/Luviskol
74	46.5	0.81586	6.88	1094.3	1.41	0.01	27.03	0.74	N_2/Luviskol
75	83.5	0.00142	4.32	1091.3	1.52	0.08	0.08	0.18	N_2/Luviskol
76	94.2	0.01263	6.39	1093.9	1.66	0.09	0.72	0.40	N_2/Luviskol
77	109.4	0.05917	4.47	1091.6	1.53	0.09	4.24	0.48	N_2/Luviskol
78	137.8	0.13652	4.50	1091.6	1.33	0.11	14.12	0.60	N_2/Luviskol
79	129.8	0.29102	5.48	1093.0	1.53	0.08	24.66	0.67	N_2/Luviskol
80	471.9	0.00025	4.06	1090.9	1.44	0.43	0.08	0.08	N_2/Luviskol
81	406.8	0.00293	4.96	1092.3	1.47	0.37	0.81	0.32	N_2/Luviskol
82	481.2	0.01299	4.48	1091.6	1.72	0.44	3.64	0.42	N_2/Luviskol
83	409.3	0.04567	5.09	1092.6	1.79	0.36	10.44	0.51	N_2/Luviskol
84	422.9	0.09045	5.35	1092.9	2.05	0.35	18.65	0.58	N_2/Luviskol
85	15.1	0.00787	4.22	1071.3	1.31	0.01	0.09	0.32	N_2/Luviskol
86	20.2	0.05875	3.99	1070.9	1.06	0.02	1.13	0.44	N_2/Luviskol
87	20.4	0.30523	4.29	1071.4	1.04	0.01	6.01	0.48	N_2/Luviskol

Tube diameter 54.5 mm, temperature 20 °C, dynamic viscosity of the gas 1.80×10^{-5} Pa s.

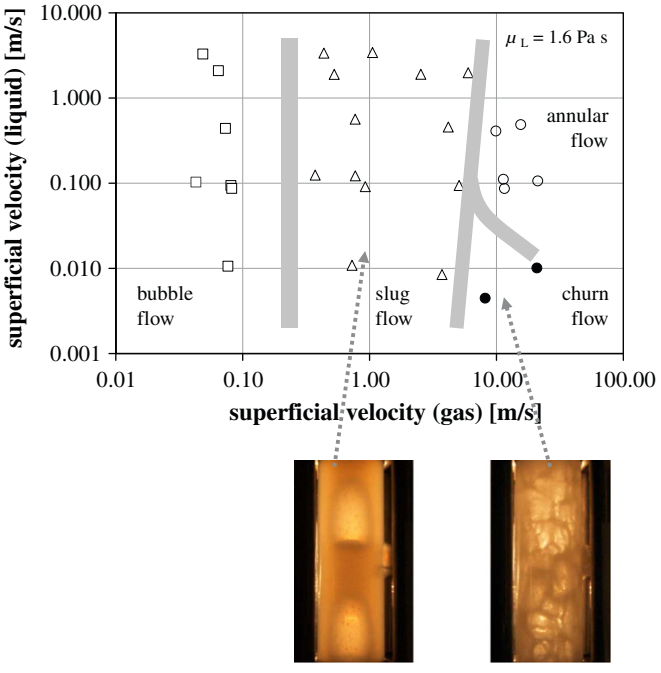

Fig. 3. Flow pattern map for two-phase flow with high liquid viscosity ($\mu_L = 1.6$ Pa s) deduced from observations in the glass test section part, see Fig. 1, as well as photographs of some typical flow regimes.

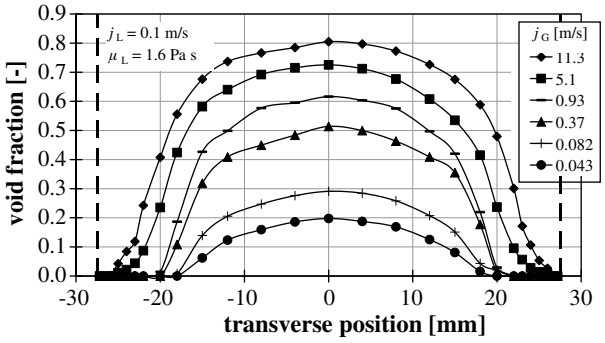

Fig. 4. Typical profiles of the line-averaged void fraction $\varepsilon_y(x)$ for a liquid viscosity of 1.6 Pa s and a superficial liquid velocity of 0.1 m/s.

polynomial in x/x_{max} instead of Eq. (6), but the results of Fig. 4 are better fitted with Eq. (6).

If Eq. (6) applies, the following radial void fraction profile (7), with the radius r_{max} equal to x_{max} (see Fig. 2) and with the same exponent m as in Eq. (6)

$$\varepsilon^*(r) = \varepsilon^*_{max}\left(1 - \left(\frac{r}{r_{max}}\right)^2\right)^m \tag{7}$$

can be shown to be valid by substitution of Eq. (7) in Eq. (4). The local void fraction exactly in the centre axis, ε^*_{max}, can be related to $\varepsilon_{y,max}$, the line average value through the centre axis, at $x = 0$

$$\varepsilon^*_{max} = \varepsilon_{y,max}\frac{\Gamma(m+1)\cdot\sqrt{\pi}}{\Gamma(m+1.5)} \tag{8}$$

Here Γ denotes the gamma function. The quotient on the RHS is 4/3 in case $m = 1$. Since ε^*_{max} should be less or equal to 1, Eq. (8) offers a constraint on m when the profile (6) is fitted to data. In addition, the exponent m must satisfy Eq. (9), which follows from the integration of Eq. (7) from the centre axis, where $\varepsilon^* = \varepsilon^*_{max}$, to r_{max}, where $\varepsilon^* = 0$, in order to obtain the cross-sectional averaged void fraction ε

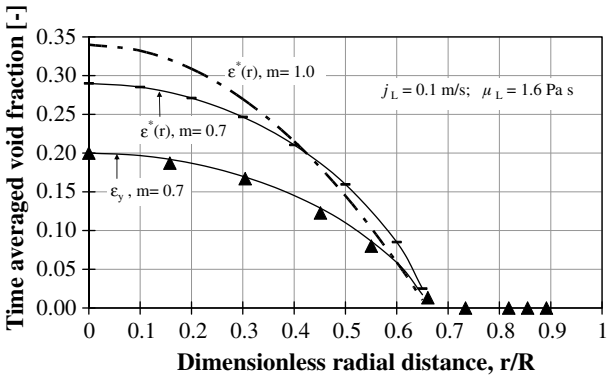

Fig. 5. Measured line averages of void fraction for $j_G = 0.043$ m/s, local void fraction profile obtained by fitting the curve $(1 - (r/r_{max})^2)^m$, and hypothetical local void fraction profile (dotted) with the same mean void fraction ε but with $m = 1.0$ to show what is meant with "peaking in the core".

$$m = -1 + (\varepsilon^*_{max}/\varepsilon)(r_{max}/R)^2 \tag{9}$$

With a sufficient degree of accuracy the measured void fraction profiles of Fig. 4 can be described by the functional relationship given by Eq. (6), see the example of Fig. 5. All the parameters involved, viz. the void fraction in the centre, the exponent m and the maximum radius r_{max}, depend on the mean superficial gas velocity $j_G = Q_G/A$ with A the cross-section area $\pi D^2/4$, $D = 2R$ with $R = 0.02725$ m, Q denotes the volumetric flow rate. In particular, for $j_L = Q_L/A = 0.1$ m/s and for $\mu_L = 1.6$ Pa s it is found that

$$\varepsilon_{max} = 0.7304 - 0.0058\ j_G \tag{10}$$

$$\frac{r_{max}}{R} = \sqrt{\alpha + \beta \cdot \sqrt{j_G}} \tag{11}$$

$\alpha = 0.408 \pm 0.01$, $\beta = 0.18175 \pm 0.08$ with $r^2 = 0.99$, $F = 510$ and j_G in m/s.

The following relation is a linear fit of the m-values, for the same conditions, that is accurate for lower j_G-values and somewhat underestimates m for the highest j_G-values measured

$$m = 0.7 + 0.027\ j_G \tag{12}$$

With increasing superficial gas velocity m increases, which implies that the gas phase becomes more concentrated in the core region of the tube. This so-called core peaking is exemplified by the curve with exponent $m = 1$ in Fig. 5, and is also observable in Fig. 4 already. The above fitting findings will be used in the following section, where the consequences for the velocity profile will be investigated.

The void fraction profiles we measured in water–nitrogen flows are much flatter, i.e. with m-values that are less than half those given by Eq. (12).

3.3. The dependence of the velocity distribution on superficial gas velocity

Analogous to the void distribution, the velocity distribution can be described by a function of radial distance, r, for time-averaged axisymmetric flows. Consider the total local superficial velocity, i.e. the mean velocity of the two-phase mixture at distance r from the centre axis: $j^* = \varepsilon^*(r)v^*_G + (1 - \varepsilon^*(r))v^*_L$, with v^*_G the time-averaged local velocity of the gas, and v^*_L that of the liquid. In most flow regimes of low-viscosity mixtures both $\varepsilon^*(r)$ and the total superficial velocity, j^*, are positive, monotonic functions of radial distance, r, according to measurements (Nakoryakov and Kashinsky, 1981; Herringe and Davis, 1976; Serizawa et al., 1975). Only low viscosity, low quality bubbly mixtures may exhibit void peaking near the wall (Žun et al., 1993). Our measurements of void fraction distributions in high-viscosity mixtures have been found to yield only positive, monotonic functions of r. It therefore stands to reason to expect j^* to be a positive, monotonic function of r also. The following profile for j^* is therefore examined now:

$$j^*(r) = j^*_{max}\left(1 - \left(\frac{r}{r_{max}}\right)^2\right)^p \tag{13}$$

It is noted that Zuber and Findlay (1965) in the article where they introduced the distribution parameter

$$C_0 = \frac{\langle \varepsilon^* \cdot j^* \rangle}{\langle \varepsilon^* \rangle \cdot \langle j^* \rangle} \tag{14}$$

considered a similar set of functions, although the generating relation they used was less general than Eq. (13). Values of r_{max} in Eq. (13) should in principle be different from those for $\varepsilon^*(r)$ in Eq. (7), but since most r_{max}-values are close to R anyway, and since viscous liquid velocities are small near the wall, differences are taken to be negligible for the analysis of trends that will now be carried out.

The definition (14) of the distribution coefficient suggests that if both the ε^*-profile and C_0 are known, the velocity profile of j^* can be deduced if j^* is a monotonic, positive function. In Section 5, it will be shown that $C_0 = 1.218 j^{-0.246} + 1$ for the high-viscosity flow considered here. Now it can be shown from Eqs. (7), (13) and (12) that

$$p = -1 + m/\{(m+1)/[C_0(r_{max}/R)^2] - 1\} \tag{15}$$

For $j_L = 0.1$ m/s, it follows that exponent p varies linearly from 1 to about 4: $p \cong 1 + 0.35 \cdot j_G$ for the high-viscosity flow at $\mu_L = 1.6$ Pa s. With increasing superficial gas velocity, the profile of the total superficial velocity becomes more peaked in the centre of the tube, see the example with $m = 1$ in Fig. 5. At high superficial gas velocity, j_G, the core of the fluid–gas mixture in the pipe is moving at high velocity whereas the region close to the wall is hardly moving at all. At low j_G the velocity profile is more flat. This trend remains the same if the profile given by Eq. 13 is replaced by other monotonic, positive functions.

The same dependency of the core peaking on superficial gas velocity is also found for the low-viscosity water–nitrogen case, but the peaking in the centre is much less pronounced in this case. The peaking in the high-viscosity case is probably a consequence of the no-slip condition at

the wall and the viscosity. The near-wall mixture hardly moves while the mixture in the core is transported fast.

4. Mean void fractions: results and comparison with existing correlations

In total, 87 data points have been collected, each one yielding a time and cross-sectional averaged void fraction of the two-phase flow, see Table 2. In this section, mean void fractions will be presented and compared with predictions using well-established correlations from the literature.

In Fig. 6, the dependence of the average void fraction on liquid viscosity is shown for a superficial liquid velocity of $j_L = 0.1$ m/s. The void fraction decreases with increasing viscosity as a result of a decreasing liquid velocity of the viscous phase adjacent to the wall, thus requiring a larger part of the cross section.

In Figs. 7–10 the experimentally determined void fractions are compared to several slip flow models. The variance of the absolute, relative and logarithmic deviations between experimental and calculated data are given as well as the standard deviations of these parameters; see Appendix for definitions. Dotted lines are given in these Figures that indicate calculated values that are 100% off from the measured values. The model of Lockhart and Martinelli (1949) shows the smallest discrepancies, see Fig. 7. Since Premoli et al. (1971) have fitted their equations to experiments with liquids of moderate viscosity only, they are not suitable to be used for the high viscosities in our tests (Fig. 8). The Chisholm model (1962,1983) tends to underpredict the void fractions for $\varepsilon < 0.4$, whereas for larger ε the model overestimates the measured values (Fig. 9). Too large void fractions are calculated with the equations of Claxton et al./HTFS (1972). This model is not suitable to describe experiments with high liquid viscosities

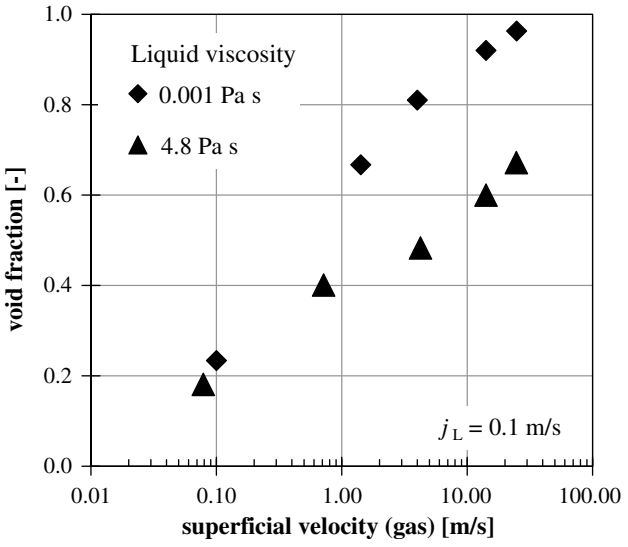

Fig. 6. Average void fraction as a function of superficial gas velocity for mixtures of nitrogen and water ($\mu_L = 0.001$ Pa s) and nitrogen with Luviskol ($\mu_L = 4.8$ Pa s).

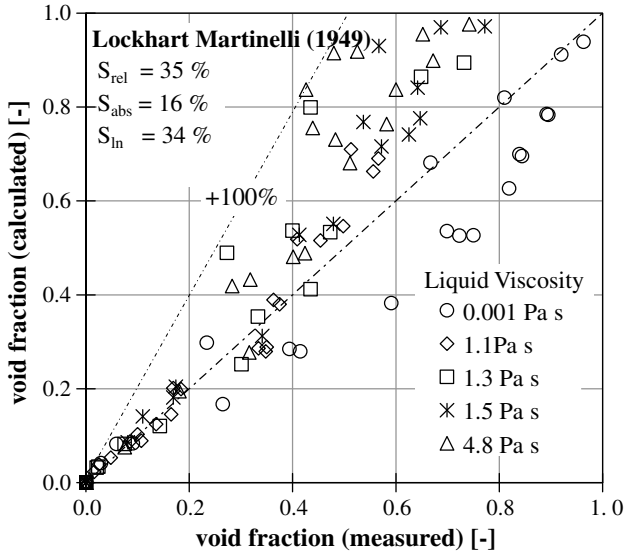

Fig. 7. Comparison of the void fraction calculated according to the model of Lockhart and Martinelli (1949) with new experimental data.

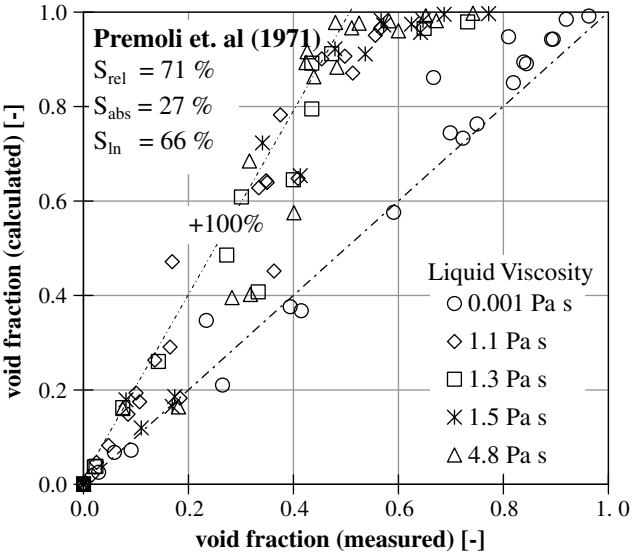

Fig. 8. Comparison of the void fraction calculated according to the model of Premoli et al. (1971) with new experimental data.

(Fig. 10). In contrast to these findings, the calculated values for water are in most cases too low.

It is concluded that none of the correlations available in the literature can predict the measured void fractions for high liquid viscosities (between 1 and 7 Pa s). Two new prediction methods have therefore been derived in order to account properly for high liquid viscosities. They are described in Section 5.

5. Mean void fraction: new prediction methods

The first new prediction method for the mean void fraction is based on the so-called drift flux correlation, defined by Zuber and Findlay (1965). They proposed a local drift

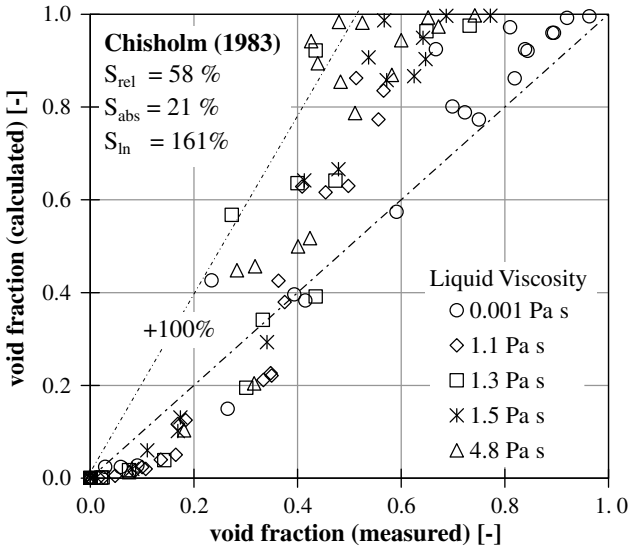

Fig. 9. Comparison of the void fraction calculated according to the model of Chisholm (1983) with new experimental data.

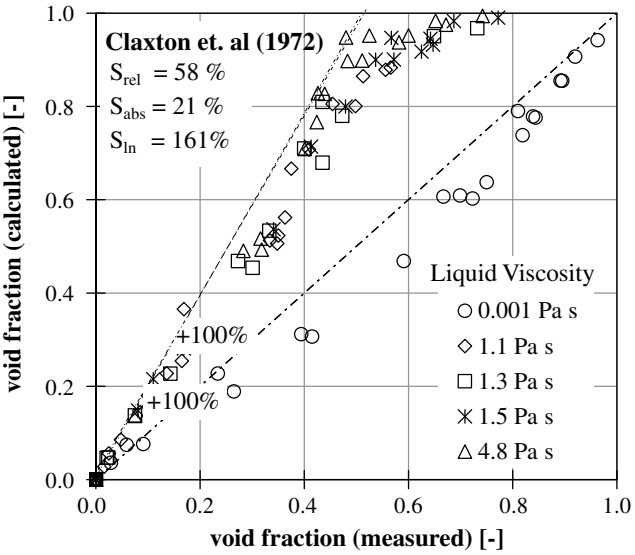

Fig. 10. Comparison of the void fraction calculated according to the model of Claxton et al. (1972) with new experimental data.

velocity u_D^* to relate the (unknown) local, instantaneous velocity of the gas phase, u_G^*, to the measurable total superficial velocity, j^*

$$u_G^* = j^* + u_D^* \tag{16}$$

By definition of the local superficial gas velocity, j_G^* (see Section 3.3), the local gas velocity yields

$$u_G^* = \frac{j_G^*}{\varepsilon^*} \tag{17}$$

The following relation is easily derived (see Eq. (3) for the averaging procedure):

$$\frac{\langle j_G^* \rangle}{\langle \varepsilon^* \rangle} = \frac{\langle \varepsilon^* \cdot j^* \rangle}{\langle \varepsilon^* \rangle} + \frac{\langle \varepsilon^* \cdot u_D^* \rangle}{\langle \varepsilon^* \rangle} \tag{18}$$

With the aid of the so-called distribution parameter

$$C_0 = \frac{\langle \varepsilon^* \cdot j^* \rangle}{\langle \varepsilon^* \rangle \cdot \langle j^* \rangle} \tag{14}$$

and the "average drift velocity"

$$u_D = \frac{\langle \varepsilon^* \cdot u_D^* \rangle}{\langle \varepsilon^* \rangle} \tag{19}$$

the following well-known equation follows:

$$u_G = \frac{j_G}{\varepsilon} = C_0 \cdot j + u_D \tag{20}$$

The drift velocity, u_D, is related to the relative velocity between the two phases in the tube, but due to the way of averaging does not need to be the average relative velocity. In general, the drift velocity is significant only in mixtures with a very low total superficial velocity, e.g. bubble columns. In most measurement conditions of the present study it is negligibly small. This leads to

$$u_G = \frac{j_G}{\varepsilon} \cong C_0 \cdot j \quad \text{or} \quad C_0 \approx \frac{j_G}{\varepsilon \cdot j} \tag{21}$$

Note that u_G is not defined at a certain place if no gas is passing, but that $j_G = \varepsilon \cdot u_G$ is obviously zero there. Various authors introduced an empirical correlation for the drift velocity and an empirical correlation for the distribution parameter in order to facilitate calculation of the average void fraction from Eq. (21). In the case of homogeneous flow, the distribution parameter, C_0, is equal to 1, whereas in other flow regimes it has higher values depending on the distribution of void fraction and gas velocity. Surprisingly the drift flux model works for all flow regimes if the distribution parameter is made dependent of a parameter that might be related to the flow regime, as for example the total superficial velocity in the following.

In order to develop a new model with a wide range of application, the distribution parameter C_0 has been calculated from the experimental data including the measured mean void fractions. Fig. 11 summarizes the findings. It shows that in a low viscosity two-phase flow (nitrogen/water, $\mu_L = 0.001$ Pa s) C_0 decreases from a value of about 2 for $j = 0.1$ m/s to a value of 1 with increasing total superficial velocity. For the high-viscosity experiments, the distribution parameter tends to larger values of C_0 ($C_0 \approx 3$ for $j = 0.1$ m/s) and decreases more slowly towards the value of 1. In order to describe this behaviour a power law function is proposed

$$C_0 = \alpha \cdot j^{-\beta} + 1 \quad (j > 0) \tag{22}$$

The distribution parameter is found to vary not systematically with viscosity at $\mu_L > 1$ Pa s, i.e. the variation is in the order of the inaccuracy of the measurements. Hence, two sets of parameters for the power law function (22) have been found by least square fits to the experimental data: one for mixtures with a liquid of low viscosity ($\mu_L = 0.001$ Pa s) and a second one for liquids with dynamic viscosities larger than 1 Pa s

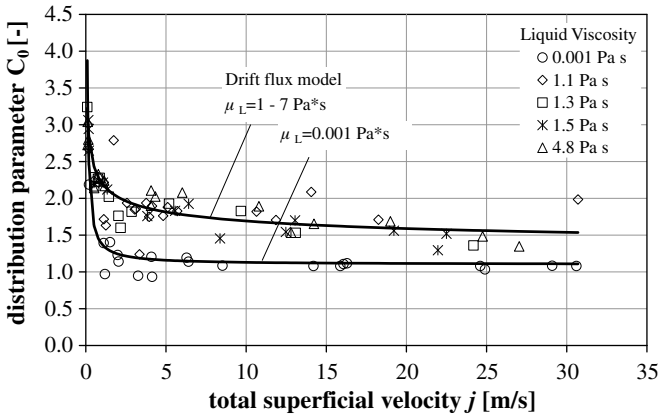

Fig. 11. Distribution parameter C_0 as a function of the total superficial velocity.

$$\alpha = 0.443 \pm 0.08, \quad \beta = 0.58 \pm 0.1, \quad r^2 = 0.99, \quad F = 683 \quad \text{for } \mu_L = 0.001 \text{ Pa s} \tag{23}$$

$$\alpha = 1.218 \pm 0.09, \quad \beta = 0.246 \pm 0.04, \quad r^2 = 0.96, \quad F = 379 \quad \text{for } \mu_L = 1\text{–}7 \text{ Pa s} \tag{24}$$

The definitions of the correlation parameters r^2 and F are given in the Appendix. The accuracy of the calculated values with the new drift flux model, Eqs. (21)–(24), is good, see Fig. 12.

As an alternative to the drift flux model, the slip S between the phases, by definition equal to the ratio of u_G to u_L, may be used to calculate the void fraction. Both models, the slip model and the drift flux model, were extensively used in the literature to correlate experimental pressure drop and void fraction data.

From definitions it follows that

$$\varepsilon = \frac{j_G}{j_L} \cdot S + j_G = \frac{\psi}{S + \psi}; \quad \text{with} \quad \psi = \frac{j_G}{j_L} \tag{25}$$

Again an empirical relation is needed, this time for the slip ratio, S. A slip correlation has been developed to calculate the void fraction at arbitrary liquid viscosity. Eq. (25) suggests that S could be a function of ψ and of some fluid properties. Hence, the following form for this relationship is selected:

$$S = 1 + \alpha \cdot \left(\frac{\mu_L}{\mu_0}\right)^{\beta} \cdot \psi^{\gamma} \quad \mu_0 = 1 \text{ Pa s} \tag{26}$$

where the 1 accounts for the expectation that the mean gas velocity exceeds the liquid velocity. Here, as well as in the following, μ_0 is taken to be 1 Pa s. The fit of α, β and γ gave a correlation coefficient, $r^2 = 0.94$ whereas the high value of the F-parameter, 1317, reflects the use of only few parameters to fit all data. See Appendix for a definition of these parameters. The values found are

$$\alpha = 1.95 \pm 0.3, \quad \beta = 0.258 \pm 0.04, \quad \gamma = 0.749 \pm 0.04, \quad r^2 = 0.94, \quad F = 1317 \tag{27}$$

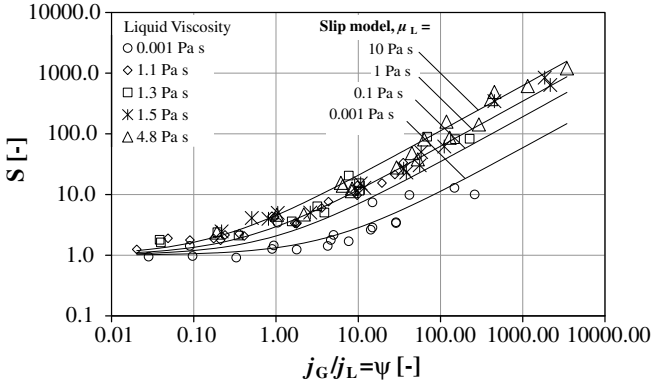

Fig. 13. Slip ratio, S, as a function of the ratio of superficial velocities, ψ.

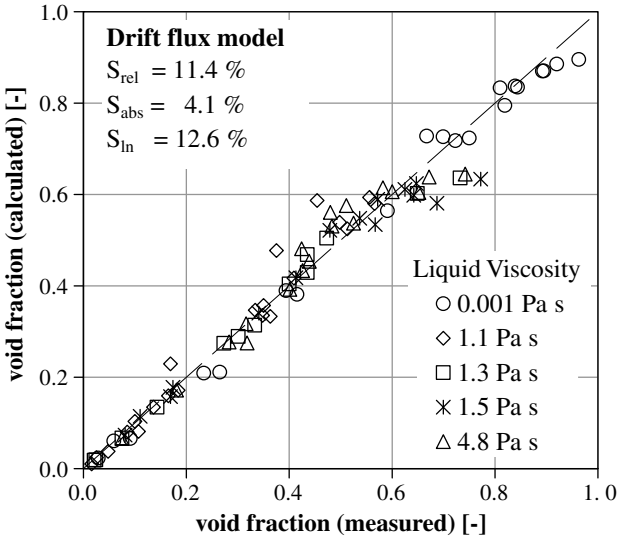

Fig. 12. Accuracy of the new drift flux model.

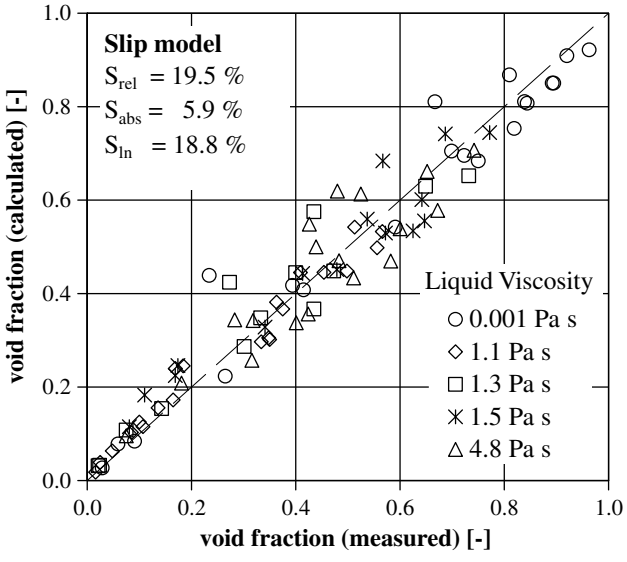

Fig. 14. Accuracy of the new slip model.

The slip correlation is compared to the experimental data in Fig. 13. Additionally, in Fig. 14 the overall accuracy of the slip model is presented. It is noted that the slip correlation for high-viscosity data reported by Chisholm (1962, 1983) also comprises a viscosity factor: $\mu_L^{0.26}$. The present data for viscosities in the range 0.001–7 Pa s are thus found to exhibit a viscosity dependence that is similar to the viscosity-dependency previously found for other viscous compounds and for other viscosity and superficial velocity ranges. Moreover, Beattie and Sugawara (1986) related the difference $(C_0 - 1)$ to the Fanning friction factor and hence to viscosity. The finding in our experiments that this difference increases with increasing viscosity is in agreement with the trend predicted by the relation of Beattie and Sugawara.

A liquid with an increased viscosity may contain micro-bubbles as tiny enclosures that are difficult to remove rapidly without heating the liquid or evacuation, see Section 3. To account for the viscosity of the liquid containing cavities, μ_{2ph}, the famous Einstein correction with mean void fraction ε can be applied

$$\mu_{2ph}/\mu_L = 1 + 2.5\varepsilon + 6.2\varepsilon^2 \tag{28}$$

It was therefore attempted to account for the micro-bubbles by substituting $\mu_{2ph} = \mu_L(1 + 2.5\varepsilon)$ for μ_L in the above fit function for S. Note that an implicit function for the void fraction is obtained in this way. However, the resulting fit gave essentially the same fit characteristics without altering the fit parameters much. It is therefore concluded that for a Luviskol mixture with a liquid viscosity up to 7 Pa s there is no need to account explicitly for the effect of micro-bubbles in the above fit function for S. Further, more detailed experiments would be necessary to get more information about micro-bubbles before their possible effect on void fraction could be assessed.

6. Conclusions

Measurements have been performed of high-viscosity two-phase flows (dynamic viscosity of the fluid up to 7 Pa s) in cocurrent upflow in a vertical tube with a wide range of mass fluxes. It has been shown that existing void fraction correlations do not predict the mean void fraction properly. Two new correlations have been presented, one based on the distribution coefficient of the drift flux model, C_0, the other based on velocity slip. It is difficult to combine the low-viscosity data (0.001 Pa s) with the high-viscosity data (1–7 Pa s) because distribution phenomena are different. Analysis of void fraction profiles and measured distribution coefficients shows that the total superficial velocity is pronouncedly peaking in the centre of the tube for the high-viscosity case, and that this core peaking is stronger for higher superficial gas velocities. The distribution coefficient of the high-viscosity data is substantially higher (about 50%) than that of the low-viscosity (water) data, with little dependency on viscosity within the viscosity regime measured. For these reasons, the first new correlation, the one in terms of C_0, has been split into two parts: one for each viscosity regime. The second correlation, in terms of slip, does unify the data for all viscosities, but at the expense of less good fitting characteristics. However, the resulting fitting parameter $\mu^{0.26}$ contains an exponent (with an inaccuracy of 0.02) that is the same as the one reported by Chisholm (1983) for oil mixtures with viscosities up to 300 mPa s. It is therefore likely that the void distribution phenomena in the measurements of Chisholm were the same as the ones reported in the present study.

Appendix. Definition of statistical numbers

Several new correlations have been examined with parameters that were fitted to the measured void fraction data. The required nonlinear least-squares procedure has been performed with Sidewrite™ and with the Gauss–Newton optimization tools of Matlab™. All errors indicated are for a 95% confidence interval.

Estimates for the accuracy of the fit have been obtained from quantifiers described below, and from a qualitative analysis of the dependency on viscosity of the residuals of the fit. If a systematic dependency was detected in the residuals, the fit was rejected. The correlation coefficient r^2 is defined by

$$r^2 = \sum_{i=1}^{N}(\hat{y}_i - \bar{y})^2 \Big/ \sum_{i=1}^{N}(y_i - \bar{y})^2$$

where N is the number of measurements with outcome y_i (void fraction), $\hat{y}_i$ are the corresponding predictions with the fit function, and is the average of the set $\{y_i\}$. The number of parameters used in the fit, k, of course affects the quality of the fit. Whereas the correlation coefficient should preferably have a value close to 1, the parameter F should at the same time have a maximum value

$$F = \left\{ \sum_{i=1}^{N}(\hat{y}_i - \bar{y})^2 \Big/ \sum_{i=1}^{N}(y_i - \hat{y}_i)^2 \right\} \cdot (N-k)/(k-1)$$

Other familiar quantifiers of fit inaccuracies, such as

$$s^2 = \sum_{i=1}^{N}(\hat{y}_i - y_i)^2/(N-k-1)$$

Table 3
Definition of statistical numbers used to characterize the predictive accuracy of a model

Statistical number	Deviation	Definition
Variance of absolute deviations	$X_{i,abs} = \varepsilon_{i,\,exp} - \varepsilon_{i,calc}$	$S_{abs} = \sqrt{\frac{\sum_{i=1}^{N} X_{i,abs}^2}{N-k-1}}$
Variance of relative deviations	$X_{i,rel} = \frac{\varepsilon_{i,exp} - \varepsilon_{i,calc}}{\varepsilon_{i,exp}}$	$S_{rel} = \sqrt{\frac{\sum_{i=1}^{N} X_{i,rel}^2}{N-k-1}}$
Variance of logarithmic deviations	$X_{i,ln} = \ln\frac{\varepsilon_{i,exp}}{\varepsilon_{i,calc}}$	$S_{ln} = exp\left\{\sqrt{\frac{\sum_{i=1}^{N} X_{i,ln}^2}{N-k-1}}\right\} - 1$

are also used; they are summarized in Table 3. The average predictive accuracy of the models is based on the values obtained for the variance of the logarithmic deviations between the experimental and calculated values, Table 3. The advantages of using these parameters were already discussed by Govan (1988) and Friedel (1981). These parameters have proven to give a balanced description of the merits of a correlation.

References

Beattie, D.R., Sugawara, S., 1986. Steam-water void fraction for vertical upflow in a 73.9 mm pipe. Int. J. Multiphase Flow 12, 641–653.

Chisholm, D.A., 1962. The influence of viscosity and liquid flow rate on the phase velocities during two-phase flow. NEL Report no. 33, East Kilbride Glasgow.

Chisholm, D.A., 1983. Two-phase Flow in Pipelines and Heat Exchangers. George Godwin, London/New York.

Claxton, K.T., Collier, J.G., Ward, J.A., 1972. HTFS correlations for two-phase pressure drop and void fraction in tubes, HTFS (Heat Transfer and Fluid Flow Service, Harwell, GB) design report 28 (AERE-R 7162).

Cormack, A.M., 1983. Computed tomography: some history and recent developments. In: Shepp, L.A. (Ed.), Computed Tomography, Proceedings of Symposia on Applied Mathematics, vol. 27, The American Mathematical Society, pp. 35–42.

Diener, R., Friedel, L., 1998. Reproductive accuracy of selected void fraction correlations for horizontal and vertical upflow. Forsch. Ingenieurwes. 64, 87–97.

Farrell, E.J., 1981. Tomographic imaging of attenuation with simulation correction for refraction. Ultrason. Imag. 3, 144–163.

Friedel, L., 1981. Kriterien für die Beurteilung der Vorhersagegenauigkeit von halbempirischen Berechnungsmodellen (Criteria for the evaluation of the predictive accuracy of half empirical models). Chem. -Ing. -Tech. 53, 59–62.

Fukano, T., Furukawa, T., 1998. Prediction of the effects of liquid viscosity on interfacial shear stress and frictional pressure drop in vertical upward gas–liquid annular flow. Int. J. Multiphase Flow 24, 587–603.

George, D.L., Shollenberger, K.A., Toczynski, J.R., O'Hern, T.J., Ceccio, S.L., 2001. Three-phase material distribution measurements in a vertical flow using gamma-densitometry tomography and electrical-impedance tomography. Int. J. Multiphase Flow 27, 1903–1930.

Govan, A.H., 1988. A note on statistical methods for comparing measured and calculated values, HTFS RS767-1, pp. 315–323.

Herringe, R.A., Davis, M.R., 1976. Structural development of gas–liquid mixture flows. J. Fluid Mech. 73, 97–123.

Kabir, C.S., Hasan, A.R., 1990. Performance of a two-phase gas/liquid flow model in vertical wells. J. Petrol. Sci. Eng. 4, 273–289.

Lockhart, R.M., Martinelli, R.L., 1949. Proposed correlation of data for isothermal two-phase, two-component flow in pipes. Chem. Eng. Prog. 45, 39–48.

Mayinger, F., 1982. Strömung und Wärmeübergang in Gas-Flüssigkeits-Gemischen. Springer-Verlag, Wien, New York.

McNeil, D.A., Stuart, A.D., 2003. The effects of a highly viscous liquid phase on vertically upward two-phase flow in a pipe. Int. J. Multiphase Flow 29, 1523–1549.

Nakoryakov, V.E., Kashinsky, O.N., 1981. Local characteristics of upward gas–liquid flows. Int. J. Multiphase Flow 7, 63–81.

Premoli, A., Di Francesco, D., Prina, A., 1971. A dimensionless correlation for determining the density of two-phase flow measures. Termotechnico 25, 17–25.

Serizawa, A., Kataoka, I., Michiyoshi, I., 1975. Turbulence structure of air-water bubbly flow II Local properties. Int. J. Multiphase Flow 2, 235–246.

Shollenberger, K.A., Roczynski, J.R., Adkins, D.R., O'Hern, T.J., Jackson, N.B., 1997. Gamma-densitometry tomography of gas holdup spatial distribution in industrial-scale bubble columns. Chem. Eng. Sci. 52, 2037–2048.

Spedding, P.L., Woods, G.S., Raghunathan, R.S., Watterson, J.K., 1998. Vertical two-phase flow, part I – part III. Trans IChemE 76, part A, 612–634.

Spisak, W., Idzik, J., 1994. Gas hold-up in stalactite and slug flows with highly viscous liquids. Chem. Eng. J. 56, B79–B85.

Taitel, Y., Bornea, D., Dukler, A.E., 1980. Modelling flow pattern transition for steady upward gas–liquid flow in vertical tubes. AIChE J. 26, 345–354.

van der Geld, C.W.M., 1987. Inferences, measurement and prediction of radial void fraction distributions. European Two-Phase Flow Group Meeting, paper I2, Report WOP-WET 87002, Eindhoven University of Technology, pp. 1–32.

Zuber, N., Findlay, J.A., 1965. Average volume concentration in two-phase flow systems. J. Heat Transfer 87, Trans. ASME, 453–468.

Žun, I., Kljenak, I., Može, S., 1993. Space–time evolution of the nonhomgeneous bubble distribution in upward flow. Int. J. Multiphase Flow 19, 151–172.